CMS Draft Analysis Note

The content of this note is intended for CMS internal use and distribution only

2021/11/20
Archive Hash: 7902af2-D
Archive Date: 2021/11/20

B meson R_{AA} and Cross Section Ratios in pp and PbPb Collisions at 5.02 TeV

Zhaozhong Shi[1], Maria Faria[2], [1], Ran Bi[1], Nuno Leonardo[2], and Yen-Jie Lee[1]

[1] Massachusetts Inst. of Technology
[2] Técnico Lisboa

Abstract

Your abstract here. (One paragraph; max length roughly 200 words (longer will be truncated for EPJC submissions). Absolute max (at arXiv) is 1920 characters.)

This box is only visible in draft mode. Please make sure the values below make sense.

PDFAuthor: “376“377“000Z“000h“000a“000o“000z“000h“000o“000n“000g“000“040“000S“000h“000i“
“000J“000i“000e“000“040“000L“000e“000e
PDFTitle: “376“377“000B“000“040“000m“000e“000s“000o“000n“000“040“000R“000A“000A“000“04
PDFSubject: “376“377“000C“000M“000S
PDFKeywords: “376“377“000C“000M“000S“000,“000“040“000y“000o“000u“000r“000“040“000t“000o“000

Please also verify that the abstract does not use any user defined symbols

Contents

1 Introduction

Relativistic heavy ion collisions allow the study of quantum chromodynamics (QCD) at high energy densities and temperatures. Under such conditions, a state in which quarks and gluons are the relevant degrees of freedom, the quark-gluon plasma (QGP) [**? ?**], is formed [**?**] as predicted by lattice QCD calculations [**?**]. Multiple probes are necessary for characterizing the properties of the QGP medium. Among these, heavy quarks, which are abundantly produced at the CERN LHC, have the potential of providing novel insights into QCD calculations, serving as probes of the QGP [**? ?**]. As they traverse the QGP, these hard-scattered partons lose energy by means of elastic collisions and medium-induced gluon radiation [**? ? ? ?**]. The study of parton energy loss can provide insights into the energy density and diffusion properties of the QGP. The full reconstruction of beauty and charm gives access to their four-momenta and allows the study of the flavor and mass dependences of such processes.

In particular, beauty quarks are consider as a golden hard probes to study the transport properties of QGP. Beauty quarks are pre produced in the early stage of heavy-ion collisions. They retain their identities and traverse through the QGP before hadronization and decay. They record the entire evolution of the QGP. From the studies of the production cross sections and nuclear modification factor of b hadrons cross section in pp and heavy-ion collisions, we can understand the energy loss mechanism of beauty quarks in the QGP medium. From the ratios of the production yield of Λ_b and B_s^0 to B^+ from low multiplicity pp, to PbPb, we can understand the beauty hadronization mechanism from small to large systems and test the QCD factorization theorem. These, along with the studies of charm and light flavor hadrons, will allow us to understand the flavor dependence of energy loss and probe the microscopic structure of QGP.

In this analysis, we will perform the measurements of B_s^0 and B^+ cross section as functions of transverse momentum, rapidity, and event multiplicity and within the CMS acceptance $|y| < 2.4$ over a broad range in pp collisions at $\sqrt{s_{NN}} = 5.02$ TeV with the CMS detector. We will use the 2017 pp datasets corresponding to an integrated luminosity of 302.3 pb^{-1}. We will follow the procedures of CADI HIN-17-008 and HIN-19-011 for the analysis. The decay channel we choose for B^+ and B_s^0 measurements are $B_s^0 \rightarrow J/\psi\phi \rightarrow \mu^+\mu^-K^+K^-$ and $B_s^0 \rightarrow J/\psi K^+ \rightarrow \mu^+\mu^-K^+$. We will use the 2018 PbPb B_s^0 and B^+ measurements to obtain the nuclear modification factor and B_s^0/B^+ ratios in pp and PbPb collisions. Our results will be important to help interpret other heavy flavor experimental results and constrain theoretical model calculations.

2 Datasets and Event Selections

2.1 Datasets

This analysis is performed using the 2017 pp data at $\sqrt{s_{_{\mathrm{NN}}}}$=5.02 TeV. The Primary dataset, triggers, and event selections we use are the same with B_s analysis ongoing parallel. For more information, please check the corresponding sections on B_s analysis note (CMS AN-19-055) [?].

The pp dataset corresponds an integrated luminosity of 1.5 nb^{-1}. The analysis uses the dimuon particle datasets (*DoubleMu* PD) for pp collisions. A complete list of the used datasets can be found in Table **??**. The full name of the used datasets are as follows.

To extract pure collision events, several offline selections are applied to each event. Events are required to have at least one reconstructed primary vertex(PV). The primary vertex is formed by two or more associated tracks and is required to have a distance from the nominal interaction region of less than 15 cm along the beam axis and less than 0.15 cm in the transverse plane. For pp, an additional selection of hadronic collisions is applied by requiring a coincidence of at least 3 HF calorimeter towers, with more than 3 GeV of total energy, from the HF detectors on both sides of the interaction point. In addition to HF coincidence, a cluster compatibility filter is used in PbPb analysis. Details of these filters can be found in Section 2.2 of [?].

2.2 MC samples

This section is identical to the B_s AN. The only difference is that we use different decay channels for reconstruction of B mesons. Here we use $B^+ \rightarrow J/\psi\ K^+$ channel.

2.2.1 MC reweighting

We use dedicated method to calculate the acceptance and efficiency correction factor, by taking average over data which is described in the section. **??**. The p_T weight we get here is not used for our nominal result, since the average over data already includes the information of data p_T shape. However, the p_T weight we obtain here is used to check the robustness of the method, and will be quoted as systematics uncertainties related with the method.
The p_T spectrum of the B^+ MC was reweighted in order to match with the data. We first evaluated the raw yield of the data and MC without any p_T weight in p_T range 5-60GeV, and normalized them. Then we took the ratio of the two to get the first p_T weight distribution. This distribution is fitted with polynomials, and we found that the 4th order polynomial have the minimum $\chi 2$ among the lowest order polynomials, thus we used this as our weight function. After then, we examined the new raw yield of MC with the new weight, and compared the distributions to get a new weight functions. We iterated this twice, and we found that the first p_T weight obtained already shows good agreement with data. Thus we use that p_T weight as our weight function.
In Fig. **??**, the normalized distributions of data and MC raw yield and their ratios are presented. The second row (with 1st p_T weight) already shows reasonable agreement between data and MC. The red fit function on the top right plot is our nominal p_T weight function.

pp MC simulations are also reweighted in order to match the centrality distribution in data. On the left panel of Figure **??**, the centrality distribution of the MC simulation (red) is compared to the one in data (blue). On the right panel, MC is given the Ncoll weight and compared to the data. The unit (HiBin) on the x-axis corresponds 0.5% centrality.

In addition to the Bpt and centrality reweighting, it is known that the MB samples used for embedding pp signal MC samples (with Cymbal5Ev8 tune) has an offset in the primary vertex z position(PVz). This deviation is corrected by giving PVz weight. The procedure are shown in Fig. **??**. The overall weight is given by the ratio between the two Gaussian functions. Note that this analysis is not sensitive to the absolute value of the PV position because the reconstruction of the B^+ meson rely only on the relative distance between PV and B^+ reconstructed vertex which is presented in the following section. We tried to estimate this effect by removing this re-weighting entirely and found that the difference is only 1.3%.

3 B^+ meson reconstruction

In this section, the B^+ meson reconstruction strategy is presented. The schematic diagram of the workflow is shown in Fig. 1, starting from muons and tracks to B^+ meson candidates. Muon candidates and tracks are required to pass several quality selection criteria as described in Section 3.1 and Section 3.2. J/ψ candidates are reconstructed by vertexing muon pairs with opposite charge, using KinematicConstrainedVertexFitter. The B^+ candidates are built by combining the J/ψ candidates with each of the selected tracks. Finally, a kinematic fit to the J/ψ-K^+ system is performed, forcing the mass of dimuon pair to be equal to to the nominal J/ψ mass based on PDG [**?**]. The selection criteria of the B^+ candidates are described in Section 4.

Figure 1: Schematic diagram of the B meson reconstruction workflow

3.1 Muon and J/ψ selection

We applied the same muon selection on B^+ with B_s^0 which is written exclusively on B_s^0 AN [**?**].

3.2 Track selection

The track selection we applied are the same with B_s^0 AN [**?**].

4 B^+ meson selection

The selections described in the previous section (so-called prefilter) are not sufficient to distinguish signal from background, especially at low p_{T} range where the entire spectrum is dominated by combinatorial backgrounds which arises from random combination of muons and tracks. In order to see clear signals and reduce the uncertainties, several additional selection on the B^+ decay topology were then applied. A cut optimization procedure was performed to decide the cut values. For more details, see Section 4.1.

4.1 Cut optimization

The goal of the optimization procedure is to maximize the statistical significance of the signals while keeping reasonably high signal efficiencies. The optimal cut that minimizes background efficiency for a specific signal efficiency is obtained by the TMVA(Toolkit for Multivariate Data Analysis with ROOT) [**?**].
Boosted Decision Tree(BDT) is chosen to be the classification method in TMVA training for B^+. In addition, for comparison the CutsGA (Genetic algorithm-based rectangular cut decision) is also examined. We found that in the lowest p_{T} bin(5-7GeV), the prefilter itself does not filter out background sufficiently, which limits the performance of BDT method. In order to enhance the performance, we first found the optimal rectangular cuts from CutsGA method in this p_{T} bin. After then we used normalized decay length(dls3D) and cosθ(2D angle between B^+ meson displacement and B^+ meson momentum in transverse plane) cuts (dls3D>12.0 cosθ >0.95; this is slightly looser than the optimal rectangular cuts, in order not to reject possible signals that BDT can reconstruct but CutsGA cannot) in our prefilter for BDT training. This enhanced the raw yield extraction and reduced the yield error. We also applied this strategy to the p_{T} 7-10 GeV/c bin with the selection (dls3D>9.0 cosθ >0.92) to enhance the performance. For other p_{T} bins, we just used the original prefilter for our BDT training.
The reconstructed candidates matched to the generated signal in MC sample are used as signal when training, while the reconstructed candidates in sideband ($0.15\ \mathrm{GeV/c^2} < |M_{B^+} - M_{B^+}^{PDG}| < 0.25\ \mathrm{GeV/c^2}$) of data sample are used as background.

The kinematic variable distributions of daughter tracks and B^+ mesons before and after applying the prefilter is shown on Figure 2, 3, 4, 5

Plots/CutOpt/KinematicsDis/Bmu1pt_0.png

Plots/CutOpt/KinematicsDis/Bmu1pt_1.png

Plots/CutOpt/KinematicsDis/Bmu1eta_0.png

Plots/CutOpt/KinematicsDis/Bmu1eta_1.png

Plots/CutOpt/KinematicsDis/Bmu1phi_0.png

Plots/CutOpt/KinematicsDis/Bmu1phi_1.png

Figure 2: The normalized $J/\psi\ \mu^-$ kinematic variable distributions before and after prefilter for p_{T} = 7 - 10 GeV/c (left) and 10 - 50 GeV/c (right) are shown above.

Plots/CutOpt/KinematicsDis/Bmu2pt_0.png Plots/CutOpt/KinematicsDis/Bmu2pt_1.png

Plots/CutOpt/KinematicsDis/Bmu2eta_0.png Plots/CutOpt/KinematicsDis/Bmu2eta_1.png

Plots/CutOpt/KinematicsDis/Bmu2phi_0.png Plots/CutOpt/KinematicsDis/Bmu2phi_1.png

Figure 3: The normalized $J/\psi\ \mu^{+}$ kinematic variable distributions before and after prefilter for p_{T} = 7 - 10 GeV/c (left) and 10 - 50 GeV/c (right) are shown above.

Plots/CutOpt/KinematicsDis/Btrk1Pt_0.png

Plots/CutOpt/KinematicsDis/Btrk1Pt_1.png

Plots/CutOpt/KinematicsDis/Btrk1Eta_0.png

Plots/CutOpt/KinematicsDis/Btrk1Eta_1.png

Plots/CutOpt/KinematicsDis/Btrk1Phi_0.png

Plots/CutOpt/KinematicsDis/Btrk1Phi_1.png

Figure 4: The normalized K^+ track, muons, and K^+ track kinematic variable distributions before and after prefilter for p_{T} = 7 - 10 GeV/c (left) and 10 - 50 GeV/c (right) are shown above.

Plots/CutOpt/KinematicsDis/Bpt_0.png

Plots/CutOpt/KinematicsDis/Bpt_1.png

Plots/CutOpt/KinematicsDis/By_0.png

Plots/CutOpt/KinematicsDis/By_1.png

Plots/CutOpt/KinematicsDis/Bphi_0.png

Plots/CutOpt/KinematicsDis/Bphi_1.png

Figure 5: The normalized B^+ kinematic variable distributions before and after prefilter for p_{T} = 7 - 10 GeV/c (left) and 10 - 50 GeV/c (right) are shown above.

We can see that the prefilter cuts do not significantly change the distribution of the kinematic variable shapes and create potential bias. Therefore, these show that our prefilter cut is valid to use.

Then, we use the following six selection variables trained for PbPb:

- dls3D: Normalized decay length (SV PV distance), the distance between primary and B^+ decay (secondary) vertex normalized by its uncertainty
- Balpha: The angle between B^+ meson displacement and B^+ meson momentum in 3D
- Btrk1Pt: Track p_T, the transverse momentum of the track
- Bchi2cl: $\chi 2$ probability, the $\chi 2$ probability of the secondary decay vertex fitting
- Btrk1Eta: The absolute value of the track pseudorapidity
- Btrk1Dxysig: Normalized track Dxy, the transverse distance between track and the primary vertex normalized by its uncertainty

The BDT training setup for all p_{T} bins are as follows: NTree = 850, MinNodeSize=2.5%, MaxDepth=3, BoostType=AdaBoost, AdaBoostBeta=0.5, UseBaggedBoost, BaggedSampleFraction=0.5, SeparationType=GiniIndex, nCuts=20

The optimal BDT cut values are defined as the numbers which maximize the figure of merit(statistical significance) $S/\sqrt{S+B}$. Here, S is the number of signal in signal region after applying optimal cuts, while B is the number of background in signal region after applying optimal cuts. Signal region is defined as $|M_{B^+} - M_{B^+}^{PDG}| < 0.08$ GeV/c^2. For the lowest p_{T} bin, we used a new figure of merit $S/\sqrt{\gamma_{quantile}(\alpha/2, S+B, 1)}$ (where, α is chosen to be 1-0.6827) that is suitable for this low signal/background ratio.

- $S = S' \times$ (signal optimal cut efficiency), where S' is the number of signal in signal region before applying optimal cuts.
- $B = B' \times$ (background optimal cut efficiency), where B' is the number of background in signal region before applying optimal cuts.

S' and B' are calculated by fitting the invariant mass plot with prefilter selection, with the same functional form used in the main analysis. However, at the 4 lowest p_{T} bins, the prefilter is not sufficient to reveal the signal. In those cases, S' is calculated by the expected number of signal from FONLL pp cross-section calculation multiplied by pre-filters efficiency, acceptance from MC, and expected R_{AA} value from previous measurement [**?**].
Fig. 6 and Fig. 7 show the correlation matrices of the training, in the lowest and highest p_{T} bin, respectively.

Plots/CutOpt/CorrelationMatrixB1.pdf Plots/CutOpt/CorrelationMatrixS1.pdf

Figure 6: TMVA training correlation matrices of PbPb in p_T 5 - 7 GeV/c.

Plots/CutOpt/CorrelationMatrixB8.pdf Plots/CutOpt/CorrelationMatrixS8.pdf

Figure 7: TMVA training correlation matrices of PbPb in p_T 50 - 60 GeV/c.

Fig. 8 shows the overtraining check in the lowest and the highest p_T bin.

Plots/CutOpt/overtrain_BDT1.pdf Plots/CutOpt/overtrain_BDT8.pdf

Figure 8: TMVA overtraining check of PbPb in p_T 5-7 and 50 - 100 GeV/c, respectively

Fig. 9 shows the variable distribution comparison between signal and background, and the statistical significance curve in p_T 15-20GeV. Some variables show prominetly distinct distribution between signal and background.

Plots/CutOpt/variables_id_c1_4.pdf

Figure 9: TMVA training variable distribution of PbPb in p_{T} 15 - 20 GeV/c.

The maximum significance point is selected as our nominal working point, as shown in Fig. 10. Tab. 1 shows the summary of the optimal selection criteria in different p_T intervals. All the other TMVA performance plots not listed in this section are on Appendix. **??**.

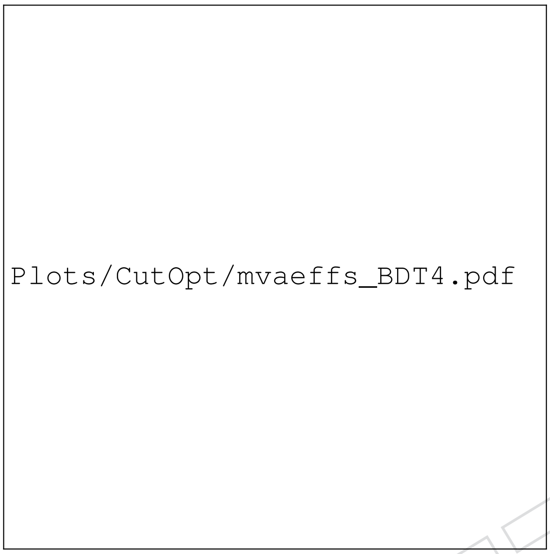

Figure 10: TMVA significance curve of PbPb in p_{T} 15 - 20 GeV/c.

p_T (GeV/c)	**5-7**	**7-10**	**10-15**	**15-20**	**20-30**	**30-40**	**40-50**	**50-60**
BDT	$>$0.02	$>$0.03	$>$0.09	$>$0.07	$>$0.10	$>$0.16	$>$0.20	$>$0.27

Table 1: Summary table of selection criteria in different p_T intervals in PbPb collisions

4.2 Fiducial region

As we go to low B^+ p_T where the daughter particles also have predominantly low p_T, it becomes improbable to detect muons in low rapidity ranges due to the limited acceptance of the muons. In other words, the signal and background candidates of B^+ are largely confined to forward rapidity region at low B^+ p_T. Fig 11 shows theoretically possible inverse of acceptance, selection efficiency, and total efficiency vs B^+ p_T and $|y|$ 2D distribution with only single muon and track selections but without BDT selections.

Plots/2DBeforeCut/Acc_0_90.pdf

Plots/2DBeforeCut/Sel_0_90.pdf

Plots/2DBeforeCut/Eff_0_90.pdf

Figure 11: The two dimensional maps of the inverse of the acceptance efficiency (left), selection efficiency (middle), and total efficiency (right) vs B^+ p_T and rapidity in MC for the centrality range of 0 - 90% without applying BDT cuts are shown above.

Next, we quantitatively examine the 2D maps of candidate distributions in both data and MC after applying the optimal BDT selections, which are shown in Fig. 12.
It is found that B^+ acceptance is better than B_s^0, presumably because of less number of tracks needed to reconstruct B meson, which allows broader phase space that the daughter particles can reside. Since this analysis is mainly for the comparison with B_s^0, we adopted more strict fiducial region ($5 < p_T < 10$GeV, $1.5 < |y_{lab}| < 2.4$) that is defined using B_s^0 2D map.

Plots/invEff/hMass2D_Cent0-90.pdf Plots/invEff/hMass2D_mc_hyperfine_Cent0-90.pd

Figure 12: B^+ p_T and rapidity two dimensional map of candidates that passed the full analysis cut in data (Left) and MC (right).

5 MC-Data Comparison

5.1 B candidate properties comparison between data and MC

Potential differences between Data and MC distributions of the variables used for the selection of the B^+ signal, can introduce biases in the efficiency corrections. In this section, the distributions of the B^+ selection variables in PbPb data and MC samples are compared.

The Splot method is used for our analysis. This is a likelihood-based method by which we reweight the data using the unbinned fit result. The weights are added to the dataset based on model and yield extraction variables. Each event has two weights: probability of belonging to the signal given its mass, probability of belonging to the background given its mass. The Splot class gives us the distributions of our variables for a given species (signal or background). The advantage of using this method is that we use the full dataset for the comparison in contrast to the sideband subtraction method where one should select the investigation range of signal and background. Furthermore, we use likelihood to describe events' behavior in contrast to the potential misidentification of signal events in background region which might occur in sideband subtraction method. For more details on general description of Splot method applied to this analysis, please refer to the section 4 and 5 of the analysis note CMS AN-19-219([**?**]).

To show the correlations between the BDT variables to the B^+ invariant mass and validate our Splot techniques approach, we first make the correlation matrices for BDT variables vs B^+ invariant mass Bmass for data and MC as follows in Figure 13:

`Plots/SPlots/CorrelationMatrixB.pdf` `Plots/SPlots/CorrelationMatrixS.pdf`

Figure 13: The correlation matrices in data (left) and MC (right) are shown above.

Fig. 14 shows the data and MC comparison results based on Splot method. Here, we focus on BDT values that are directly used in our signal extraction and related to MC distribution validation, rather than the variables themselves used in BDT training. In a wide ranges of BDT, the two distributions show good agreement. We only focus on the region where BDT is greater than the working point and is smaller than the maximum value that candidates have.

Plots/SPlots/BDT_pt_5_7_mc_validation_Bu.pdf

Plots/SPlots/BDT_pt_7_10_mc_validation_Bu.pdf

Plots/SPlots/BDT_pt_10_15_mc_validation_Bu.pdf

Plots/SPlots/BDT_pt_15_20_mc_validation_Bu.pdf

Plots/SPlots/BDT_pt_20_30_mc_validation_Bu.pdf

Plots/SPlots/BDT_pt_30_40_mc_validation_Bu.pdf

Plots/SPlots/BDT_pt_40_50_mc_validation_Bu.pdf

Plots/SPlots/BDT_pt_50_60_mc_validation_Bu.pdf

6 Signal Extraction

The method and the fit model for signal and background we applied are mostly the same with B_s AN. Please refer to the corresponing section in [**?**].
However, there is one major difference between B_s and B^+ yield extraction. From the inclusive J/ψ sample study, we have found that there is a clear and sizable contribution from non-prompt J/ψ candidates that are fed down from the B^+ signal in our region of interest. We model this component with an error function and a Gaussian. The error function component mostly comes from 4-prong B meson decay (e.g. $B^+ \rightarrow J/\psi\, K^*(892)^+$) that are partially reconstructed as $B^+ \rightarrow J/\psi\, K^+$ (one track is lost) and can form peaking structures for values of the invariant mass below $\approx$5.20 GeV/c^2. The Gaussian contribution mainly comes from $B^+ \rightarrow J/\psi\, \pi^+$ where pion is misidentifieds as kaon.
The ratio of the height of error function and the Gaussian is fixed by MC simulation. However, the Gaussian component is shown to be relatively negligible compared to the error function, and even more to the signal double Gaussian of our nominal channel. More details on the non-prompt J/ψ study can be found in Appendix Sec. A.
Note that we do not discriminate B^+ from B^- in raw yield extraction process. Therefore, the invariant mass plots shown below contains both B^+ and B^- signal and backgrounds. This double counting is properly canceled in the corrected yield calculation process later.

In Fig. 15 and Fig. 16, the invariant mass spectra and their pull distributions obtained in the p_T intervals in the PbPb analyses are presented.

We also make the comparison between the symmetric raw yield error and their asymmetric upper and lower yield error using the RooFit framework on the unbinned fit. The table is shown below in Table 2:

Table 2: The comparison between RooFit and unbinned fit framework.

Centrality	p_T (GeV/c)	Raw Yield Error	RawYield Error Up	Raw Yield Error Down
0 - 90%	7 - 10	10.88	11.20	10.66
0 - 90%	10 - 15	20.68	21.05	20.35
0 - 90%	15 - 20	17.86	18.21	17.56
0 - 90%	20 - 50	19.84	20.19	19.55
0 - 30%	10 - 50	27.72	28.01	27.45
30 - 90%	10 - 50	19.53	19.92	19.20
0 - 90%	10 - 50	33.78	34.13	33.47

Figure 15: Invariant mass distribution of B^{+} candidates obtained in PbPb collisions in p_{T} intervals in the transverse momentum range from 7-50 GeV/c and Centrality 0-90%.

Figure 16: Invariant mass distribution of B^+ candidates obtained in PbPb collisions in centrality intervals 0 - 30%, 30 - 90%, and 0 - 90% in the transverse momentum range from 10 - 50 GeV/c.

6.1 Closure test of the fitting procedure

In order to validate the yield extraction procedure, we generate 5000 toy MC for the fit and make the pull distribution. Then we perform the Guassian fits to the pull distribution to obtain the mean and width. The results are show in Fig 17 and Fig 18:

Figure 17: The pull distribution and the Gaussian fits for 0 - 90% at 7 - 10, 10 - 15, 15 - 20, 20 - 50 are shown respectfully above.

Plots/ClosureTest/DataBoostrapFit/pull_signal_full_-1_0_90.png Plots/ClosureTest/DataBoostrapFit/pull_signal

Plots/ClosureTest/DataBoostrapFit/pull_signal_full_-1_30_90.p

Figure 18: The pull distribution and the Gaussian fits for 0 - 90% at 7 - 10, 10 - 15, 15 - 20, 20 - 50 are shown respectfully above.

We can see that all p_{T} and centrality bins have zero mean and unit width from the Gaussian fits to the pull distribution. This validate the closure of our fits to extract the B^{+} raw yield.

7 Acceptance and Efficiency

8 Closure Test of the B^+ Corrected Yield

8.1 Raw Yield Closure

8.2 Efficiency Closure

8.3 Corrected Yield Closure

9 Results

9.1 p_{T} differential corrected yield in pp collisions at 5.02 TeV

The method we applied is the same with B_s AN [**?**].

In Fig. 19, Number of MinBias events-normalized, TAA-normalized, efficiency-corrected and p_{T}-width divided yield (let's call this "normalized corrected yield") of B^+ mesons in the centrality 0-90% and rapidity region $|y_{\mathrm{lab}}| < 2.4$ (Caveat: Note the fiducial region $1.5 < |y_{\mathrm{lab}}| < 2.4$ in B^+ p_{T} 7 - 10GeV/c) in PbPb collisions at $\sqrt{s}$ =5.02 TeV is presented. The boxes around the data points represent the total systematic uncertainties.

Plots/Results/plotCrossSection/xsec_vsPt.pdf

Figure 19: B^+ normalized corrected yield vs. p_{T} in the inclusive centrality range 0-90%. (Left) B^+ analysis p_{T} bin (Right) B^0_s analysis p_{T} bin. Note the fiducial region p_{T} 5-10GeV and $1.5 < |y_{\mathrm{lab}}| < 2.4$

In addition, we provide the normalized corrected yield for inclusive p_{T} 10-50 GeV/c in 0 - 30%, 30 - 90&, and 0 -90% centrality bins in Fig. 20.

The normalized corrected yields and their uncertainties for various kinematic ranges are summarized in Table. 3 and Table. 4. For more details on systematic uncertainties, see Section. 10.

Table 3: B^+ normalized corrected yields and the uncertainties in various p_{T} ranges within centrality 0-90%. All the corrected yield values are in units of pb*c/GeV. Note that the global uncertainties are not included here on this table, which are sub 4% level. Note also the fiducial region p_{T} 5-10GeV and $1.5 < |y_{\mathrm{lab}}| < 2.4$ and the same as the B_s p_{T} binning is reported.

p_{T} (GeV/c)	Center (GeV/c)	Corr. yield (pb GeV^{-1}c)	Stat. up	Stat. down	Syst. up	Syst. down
(7,10)	8.73	331984	15.8%	15.1%	13.6%	13.6%
(10,15)	12.4	298062	7.60%	8.77%	19.1%	19.1%
(15,20)	17.2	66567.7	6.54%	6.66%	7.51%	7.51%
(20,50)	27.3	7730.12	6.64%	5.49%	6.02%	6.02%

Plots/Results/plotCrossSection/xsec_vsCent.pdf

Figure 20: B$^+$ normalized corrected yield vs. $\langle N_{part} \rangle$ in inclusive p_{T}. 10-50GeV is shown above.

Table 4: Summary table of B^+ corrected yield for different centrality bins

Centrality	Corr. yield (pb)	stat. up (+)	stat. down (-)	syst.. up (+)	syst. down (-)
0% - 30%	1918800	5.81%	5.54%	16.6%	16.6%
30% - 90%	2481820	8.22%	6.97%	13.6%	13.6%
0 - 90%	2092040	5.06%	4.54%	15.2%	15.2%

9.2 Rapidity differential corrected yield in pp collisions at 5.02 TeV

9.3 Multiplicity differential corrected yield in pp collisions at 5.02 TeV

9.4 B_s^0/B^+ ratio as a function of p_T in pp collisions at 5.02 TeV

9.5 B_s^0/B^+ ratio as a function of y in pp collisions at 5.02 TeV

9.6 B_s^0/B^+ ratio as a function of Multiplicity in pp collisions at 5.02 TeV

9.7 B-meson R_{AA} vs p_T at 5.02 TeV

9.8 B-meson R_{AA} vs y at 5.02 TeV

9.9 B-meson R_{AA} vs Multiplicity at 5.02 TeV

10 Systematic uncertainties

10.1 Summary table

Below are the summary tables of various systematic uncertainties. For detailed description of each systematics source, please refer to the subsequent subsections.

Table 5: Summary of systematic uncertainties from each factor in B^+ PbPb analysis for corrected yield vs p_T. All the values are shown in percentage.

Factors	(7,10)	(10,15)	(15,20)	(20,50)
Hadron tracking efficiency	5%	5%	5%	5%
Data-MC Discrepancy	4.17%	15.25%	3.01%	1.65%
p_T shape	0.162%	0.211%	0.010%	0.008%
PDF variation background	4.46%	2.67%	2.74%	2.36%
PDF variation signal	0.117%	0.546%	0.576%	1.03%
TnP Systematics	6.12%	9.36%	3.28%	0.34%
MC stat.	9.22%	3.36%	1.92%	1.35%
Total	13.59%	19.08%	7.51%	6.02%
N_{MB} events	1.26%	1.26%	1.26%	1.26%
T_{AA}	2.2%	2.2%	2.2%	2.2%
Branching fractions	2.9%	2.9%	2.9%	2.9%
Global Systematics	3.85%	3.85%	3.85%	3.85%

Table 6: Summary of systematic uncertainties from each factor in B^+ PbPb analysis for corrected yield vs centrality. All the values are shown in percentage.

Factors	0 - 30 %	30 % - 90%	0 - 90 %
Hadron tracking efficiency	5%	5%	5%
Data-MC Discrepancy	13.28%	8.49%	11.51%
p_T shape	0.170%	0.106%	0.154%
PDF variation background	0.412%	1.13%	0.427%
PDF variation signal	2.50%	2.57%	2.60%
TnP Systematics	7.20%	7.85%	7.43%
MC stat.	3.37%	2.26%	2.49%
T_{AA}	2.0%	3.6%	2.2%
N_{MB} events	1.26%	1.26%	1.26%
Total	16.63%	13.65%	15.24%
Branching fractions	2.92%	2.92%	2.92%
Global Systematics +)	2.92%	2.92%	2.92%
Global Systematics -)	2.92%	2.92%	2.92%

We also plot the summary plots for the table able as follows in Fig 21

Plots/Sys/Summary/BpPtSyst.png

Plots/Sys/Summary/BpCentSyst.png

Plots/Sys/Summary/BpIncSyst.png

Figure 21: The plots summarizing the systematic uncertainties for p_{T} bins and centrality bins are shown above.

10.2 T_{AA} and N_{MB}

We use the same uncertainties for T_{AA} (Nuclear overlap function) and N_{MB} (Number of Min-Bias events) listed on the B_s AN [?].

10.3 Branching ratio

The systematic uncertainty on the branching ratio of the decay $B^+ \rightarrow J/\psi\ K^+$, with $J/\psi \rightarrow \mu^+\mu^-$, is calculated by adding in quadrature the uncertainties on each sub-channel. The resulting uncertainty for the full decay chain is 2.8% [?]. This is global to all p_T and centrality selections in our analysis.

10.4 Tracking efficiency

The current standard value of tracking efficiency uncertainty for one track is 5% for now, suggested in the link `https://twiki.cern.ch/twiki/bin/viewauth/CMS/HITracking2018PbPb`. This is global to all p_T and centrality selections in our analysis. This number may be updated later.

10.5 Muon efficiency: Tag and Probe

The difference between the nominal and varied values are quoted as our systematics, and they are shown in Figure 22 and Figure 23 and Table. 5 and Table. 6.

Plots/Sys/SysSplot/total/SystTnPRatio_4Bins_0_90.png

Figure 22: The upper bound and lower bound systematic uncertainties in $\langle \frac{1}{\alpha \times \epsilon} \rangle$ vs p_T with total tag and probe correction are shown above.

Plots/Sys/SysSplot/tot...

Figure 23: The upper bound and lower bound systematic uncertainties in $\langle \frac{1}{\alpha \times \epsilon} \rangle$ vs p_T with total tag and probe correction are shown above.

According to the studies, we calculate the systematic uncertainties due to tag and probe scale factor. Table **??** and table **??** summarize the tag and probe systematic uncertainties results for p_T and centrality from our studies

However, according to the Muon POG, due to the issues in the trigger tag and probe scale factor, we have also conduct the difference between the efficiencies with and without any tag and probe scale factor correction applied. Our results for p_T and centrality are shown in Figure **??**:

The final summary of tag and probe systematic results are shown on Table **??** and **??**.

10.6 MC-Data Discrepancy

10.7 p_{T} shape: Bpt weight

The potential difference in p_{T} distributions in data and MC entails difference in calculation of efficiency correction. The B^{+} p_{T} distributions of MC can be modified by Bpt weight (shown in 2.2.1) to have closer distribution with data. The Exponential and Polynomial weight function are given by:

We quote the percentage deviation of B p_{T} weighted efficiency correction factor $\langle 1/(acc \times eff) \rangle$ from the nominal without B p_{T} weight as the systematic uncertainties. Table. **??** and Table. **??** show the systematics for differential p_{T} and inclusive p_{T}, respectively. Fig. **??** and Fig. **??** shows the comparison plots for differential p_{T} and inclusive p_{T}, respectively. Note that the systematics are very small, thus the differences may not be distinguished prominently on the plots.

We can see that the p_{T} shape systematic uncertainties on the efficiency correction have been reduced to negligible using the $\langle \frac{1}{\alpha \times \epsilon} \rangle$ approach.

10.8 MC stats: Toy MC study

The statistical uncertainties of $\langle\frac{1}{\alpha\times\epsilon}\rangle$ in MC are examined by toy MC study. From the nominal 2D map, we generated 10000 toy MCs for each rapidity p_{T} bin. The toy 2D maps are then propagated to the $\langle\frac{1}{\alpha\times\epsilon}\rangle$ data-average calculation. The distribution of data-averages are drawn in each analysis p_{T} and centrality bin, and the RMS deviation of the distribution (supposedly Gaussian) is compared to the nominal value. The ratio between RMS and the nominal value is quoted as systematics related to MC stats.

Table. **??** and Table. **??** shows the systematics for differential p_{T} and inclusive p_{T}, respectively. Fig. **??** and Fig. **??** shows the toy MC 1/(acceptance*efficiency) distributions for differential p_{T} and inclusive p_{T}, respectively. The blue markers are toy MC distribution, the red lines are the nominal correction factors in the main analysis.

10.9 Signal extraction: PDF variation

Here we quote the numbers. For plots with more details, see Appendix. **??**.
As discussed in detail in Sec. 6, the central value of the raw yields were extracted using a fit function of Double Gaussian signal and exponential combinatorial background. The non-prompt component was modeled with an error function and a Gaussian peak. The systematic uncertainty on the signal extraction was evaluated by varying the functions used to model the various components:

- Model the signal with a triple Gaussian function.
- Release the constraint on the width of the signal double Gaussian (fixed in the default fit to the MC extracted values). In this case, a scaling factor (a) between the MC widths is left as a free parameter in order to account for possible differences between the resolution in data and MC.
- Fixed the mean of the signal double Gaussian.
- Consider 1st, 2nd, and 3rd order polynomial for combinatorial background.

The detailed description on the release of the constraints on the widths of the signal double Gaussian is as follows. The full signal model used in the fit to data is:

$$\alpha \frac{1}{a\sigma_1\sqrt{2\pi}} e^{-\frac{1}{2}\frac{(B_{mass}-\mu)^2}{(a\sigma_1)^2}} + (1-\alpha)\frac{1}{a\sigma_2\sqrt{2\pi}} e^{-\frac{1}{2}\frac{(B_{mass}-\mu)^2}{(a\sigma_2)^2}}, \tag{1}$$

where a is the resolution scaling factor (the same for both gaussians) which describes the possible discepancy between data and MC fit, α is the relative proportion between the gaussians, σ_1 and σ_2 are the Gaussians' widths that are directly derived from MC fit, and μ is the mean shared by both Gaussians.
In order to examine the potential systematic difference in data and MC signal fit, we are required to define a moderate variation range of the scaling factor in order not to introduce statistical fluctuations in our estimation. To achieve this, we first performed fit by letting the scaling factor float around in individual p_{T} bins and inclusive p_{T} bin (Figure **??**). The parameter values from the best fit are summarised in Table **??**.
We observed that in several individual p_{T} bins, the deviations from unity(value for nominal fit) are sizable. In mid p_{T} bins (10-15-20-30GeV) where statistics are comparably large, the deviations are small. Whereas in low p_{T} bins(5-7-10GeV) and high p_{T} bins(30-40-50-60GeV) where statistics are small, the deviations are relatively large. On the other hand, the optimal scailing factors of individual p_{T} bins agree with that of inclusive p_{T} bin within a significance of 2 σ. From this observation, the sizable differences can be considered to mainly come from statistical limitation of each small p_{T} ranges. In addition, the 2 σ difference can be considered to be the statistical uncertainties of scaling factors of individual p_{T} bins.
To conclude, we can claim that the scaling factor of the inclusive p_{T} ($a = 1.09 \pm 0.04$) is a representative of the scaling factor for all p_{T} bins. Since that factor is a optimal fit parameter, we can take 10% variation from the nominal value(unity) as our signal PDF variation range where the fits are good enough and has reasonably low statistical uncertainties, which is desirable for systematic uncertainties estimation. Here we used jargons increased and decreased width which refers to $a = 1.1$ and 0.9, respectively.

A Non-prompt J/ψ background

In the B^+ invariant mass spectrum, there are potential background feed-down sources coming from other B meson decays that can form peaking structures in the region of interest, and need to be properly subtracted in order not to bias the yield extraction procedure. In order to estimate these components, we processed the inclusive B meson MC sample with the nominal B^+ channel workflow, and vetoed the candidates that are matched to a genuine B^+ signal. The resulting B candidate mass spectrum in the inclusive p_T range (5-100 GeV/c) is shown in Fig. 24 for PbPb MC samples.
It is clear that these sources create a peaking structure in the region of M_{inv} <5.20 GeV/c^2. This structure can be nicely fit with an error function as done previously in B proton-proton analyses [?]. In addition, there is a minor peak on the right shoulder (≈5.34 GeV/c^2) of the nominal signal (≈5.28 GeV/c^2), and this can be fit with an Gaussian function. There is additional combinatorial background which is fitted with a linear function. This contribution is absorbed in the total combinatorial background of our nominal channel of the main analysis. As described in details in Sec. 6, the shape of the Non-prompt function is used as template in the fit extraction procedure.
Further MC studies were done in order to identify the different channels that give rise to the non-prompt peaking structure in the B^+ invariant mass spectrum. Few main processes were identified:

- 4-body B^+ decays which occur via resonant decay channels e.g. $B^+ \to J/\psi\, K^*(892)^+$. In these cases, we distinguish the kaons coming from the $K^*(892)^+$ decays as coming from a signal $B^+ \to J/\psi\, K^+$ decay.
- 4-body B^0 decays channels e.g. $B^0 \to J/\psi\, K^*(892)^0$.
- $B^+ \to J/\psi\, \pi^+$ decays in which we misidentified the π^+ as a K^+.

The different contributions in PbPb are presented in Fig. 25. The contribution from $B^+ \to J/\psi\, \pi$ clearly form a peaking structure on the right shoulder of the nominal decay channel $B^+ \to J/\psi\, K^+$. However, the overall magnitude of this component is tiny compared to the other two sources, and negligible compared to the nominal signal. As a consequence, we can barely see the contribution of this peaking structure in the invariant mass plot of B^+ nominal channel.

Plots/Nonprompt/plotsPbPb/fitNP_PbPb.pdf

Figure 24: B^+ candidate mass spectrum obtained in inclusive B meson MC production after vetoing the contribution of genuine B^+ signal candidates in PbPb.

Figure 25: Peaking background contribution from $B^+ \to J/\psi\ \pi$ and from K resonant decay channels of B^0 and B^+ in PbPb MC.

Acknowledgments

References